ACS OMEGA

Open Access

http://pubs.acs.org/journal/acsodf

Article

Superstructure of $Fe_{5-x}GeTe_2$ Determined by Te K-Edge Extended X-ray Absorption Fine Structure and Te Kα X-ray Fluorescence Holography

Ritsuko Eguchi, Halubai Sekhar, Koji Kimura, Hirokazu Masai, Naohisa Happo, Mitsuki Ikeda, Yuki Yamamoto, Masaki Utsumi, Hidenori Goto, Yasuhiro Takabayashi, Hiroo Tajiri, Koichi Hayashi, and Yoshihiro Kubozono*

Cite This: *ACS Omega* 2024, 9, 21287−21297

Read Online

ACCESS | Metrics & More | Article Recommendations | Supporting Information

ABSTRACT: The local structure of the two-dimensional van der Waals material, $Fe_{5-x}GeTe_2$, which exhibits unique structural/magnetic phase transitions, was investigated by Te K-edge extended X-ray absorption fine structure (EXAFS) and Te Kα X-ray fluorescence holography (XFH) over a wide temperature range. The formation of a trimer of Te atoms at low temperatures has been fully explored using these methods. An increase in the Te−Fe distance at approximately 150 K was suggested by EXAFS and presumably indicates the formation of a Te trimer. Moreover, XFH displayed clear atomic images of Te atoms. Additionally, the distance between the Te atoms shortened, as confirmed from the atomic images reconstructed from XFH, indicating the formation of a trimer of Te atoms, i.e., a charge-ordered $(\sqrt{3} \times \sqrt{3})R30^\circ$ superstructure. Furthermore, Te Kα XFH provided unambiguous atomic images of Fe atoms occupying the Fe1 site; the images were not clearly observed in the Ge Kα XFH that was previously reported because of the low occupancy of Fe and Ge atoms. In this study, EXAFS and XFH clearly showed the local structure around the Te atom; in particular, the formation of Te trimers caused by charge-ordered phase transitions was clearly confirmed. The charge-ordered phase transition is fully discussed based on the structural variation at low temperatures, as established from EXAFS and XFH.

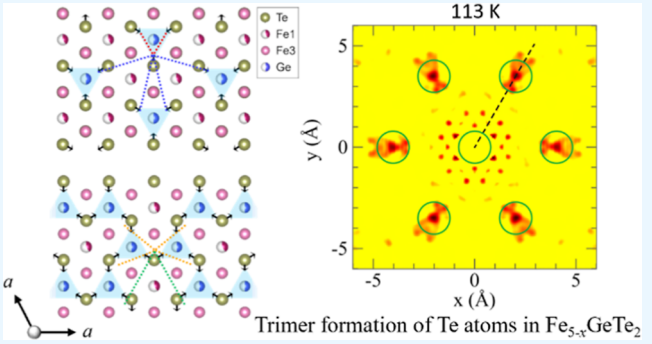

INTRODUCTION

Recently, two-dimensional (2D) layered materials have attracted attention from physicists and chemists owing to their superconductivity and topological natures.[1−24] The most scientifically important superconducting materials reported during the past two decades have been realized in 2D layered materials.[1,13−15,19,22−24] Additionally, some superconducting materials have been recognized as topological quantum materials.[9−24] Topological quantum materials such as topological insulators, topological semimetals (Dirac and Weyl semimetals), and topological metals have been found in 2D layered materials.[9−24] Thus, 2D layered materials provide an excellent platform for studying novel physical properties and topological quantum natures.

The most common topological insulator is Bi_2Se_3,[9,10] which has a bulk bandgap and gapless surface states. Topological semimetals also exhibit novel physical properties such as chiral magnetic and quantum anomalous Hall effects.[16,17] Dirac or Weyl semimetals emerge depending on the preservation of time-reversal symmetry and/or spatial inversion symmetry, and both semimetals have gapless linear dispersions near the cross points (Dirac or Weyl points) of the valence and conduction bands.[16−21] Moreover, topological Kagome metals, such as KV_3Sb_5 and CsV_3Sb_5, have been extensively studied owing to their unique superconducting properties.[22−24]

Van der Waals 2D layered materials, such as $Cr(Si,Ge)Te_3$, $Cr(Br,I)_3$, and Fe_nGeTe_2 $(2 \leq n \leq 5)$, have recently been investigated owing to the emergence of various magnetic ordered states.[25−44] In particular, Fe_nGeTe_2 $(3 \leq n \leq 5)$ is an intriguing material which exhibits ferromagnetic (FM) ordered states with a high Curie temperature (T_{Curie}) or room-temperature T_{Curie}. As n increases in Fe_nGeTe_2, the value of T_{Curie} increases to 270−310 K for $n = 5$ (or $Fe_{5-x}GeTe_2$). The temperature dependence of magnetic susceptibility M/H of $Fe_{5-x}GeTe_2$ indicates the presence of three magnetic

Received: February 13, 2024
Revised: April 12, 2024
Accepted: April 19, 2024
Published: May 1, 2024

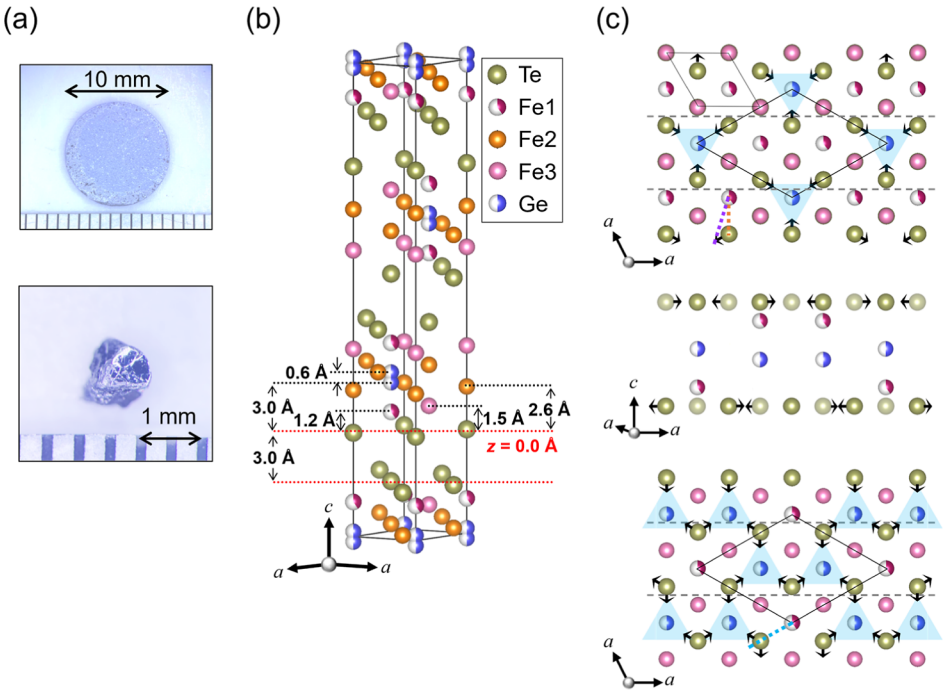

Figure 1. (a) Photographs of the pellet sample (above) and crystal (below) of $Fe_{5-x}GeTe_2$. (b) Crystal structure of $Fe_{5-x}GeTe_2$ depicted using atomic coordinates reported by May et al.[36] (c) Schematic representation of the charge-ordered $(\sqrt{3} \times \sqrt{3})R30°$ superstructure. The movement of the Te atom that is caused by the CO transition (or formation of $(\sqrt{3} \times \sqrt{3})R30°$ superstructure) is depicted using arrows. In (c), two *ab* layers (top and bottom) constitute an asymmetric unit. The ac layer corresponding to the asymmetric unit is shown in the middle of (c), in which the Fe2 and Fe3 atoms are not depicted. Three Te−Fe1 distances (r_{Te-Fe1}, $r_{Te-Fe1}(1)$ and $r_{Te-Fe1}(2)$) are provided by dashed orange, purple, and right blue lines, respectively. Fe1 is located below or above the Te plane by 1.2 Å (see Figure 7e).

transitions (paramagnetic (PM) state to FM state, FM state to FM state coexisting with charge-ordered (CO) state, and FM plus CO state to FM plus faded CO state);[41] *M* and *H* refer to the magnetization and applied magnetic field, respectively. The transition temperature from the PM to the FM state corresponds to that of T_{Curie}. The magnetic transition temperatures of the transition of FM to FM plus CO and that of FM plus CO to FM plus faded CO are referred to as T_{C2} and T_{C1}, respectively. The formation of a trimer of Te atoms in the CO state has been confirmed via scanning tunneling spectroscopy (STS) analyses of the exfoliated Te layer of a $Fe_{5-x}GeTe_2$ crystal.[40,41] Subsequently, Eguchi et al. confirmed the formation of the trimer (CO $(\sqrt{3} \times \sqrt{3})R30°$ superstructure) via Ge Kα X-ray fluorescence holography (XFH) analysis of a $Fe_{5-x}GeTe_2$ crystal.[44] The CO $(\sqrt{3} \times \sqrt{3})R30°$ superstructure was formed partially in ordered and disordered 1 × 1 structures, as described in a XFH study[44] and other studies[36,41] which used scanning transmission electron microscopy (STEM) and STS.

Herein, we investigated the Te K-edge extended X-ray absorption fine structure (EXAFS) and Te Kα XFH of a crystal of $Fe_{5-x}GeTe_2$ to elucidate the variation in the local structure around the Te atom that results from magnetic/structural transitions at low temperature. The purpose of this study was to directly observe the change in the local structure using Te K-edge EXAFS and Te Kα XFH, which should directly capture the movement of Te atoms induced by the magnetic transition, and to find the Fe atoms occupying the Fe1 site. These phenomena have never been observed in previous studies of Ge Kα XFH[44] because of the low occupancy of Fe at the Fe1 site and Ge atoms. Notably, the observation of Fe atoms at the Fe1 site, which corresponds to the Fe site above or below the Ge atom, is crucial for understanding the CO state because the presence of Fe atom is closely related to the trimer formation of Te atoms. To sum up, we could obtain the more detailed information on the formation of a Te trimer from Te Kα XFH which provided more clear atomic spots in the Te plane than previous Ge Kα XFH,[44] and the origin of the Te trimer formation could be more deeply discussed than the previous study.[44]

EXPERIMENTAL SECTION

The crystals of $Fe_{5-x}GeTe_2$ were prepared according to a previously described reaction process.[44] The same batch of samples that was used for the Ge Kα XFH measurement[44] was used in this study. The energy-dispersive X-ray (EDX) spectrum, *M*/*H*, and powder X-ray diffraction pattern confirmed the successful preparation of $Fe_{5-x}GeTe_2$, i.e., the realization of suitable sample for the measurement of the EXAFS and XFH. In addition, the Laue photograph indicated the exact exfoliation of the *ab* plane of $Fe_{5-x}GeTe_2$.[44]

The polycrystalline powder sample of $Fe_{5-x}GeTe_2$ was mixed with hexagonal BN (h-BN) to fabricate pellets of a suitable concentration and homogeneity; the pressure applied to the mixed powder for the fabrication of the pellet was ∼40 MPa, and the diameter of the pellet was 10 mm. A photograph of the pellet is shown in Figure 1a. The Te K-edge EXAFS of the pellet sample of $Fe_{5-x}GeTe_2$ was measured in transmission mode at BL14B2 of SPring-8; the K-edge of Te was ideally 31.824 keV. The pellet sample was introduced into a low-temperature cryostat to lower the temperature. The EXAFS data were analyzed using the analysis programs, ATHENA and ARTEMIS, to clarify the local structure around the Te atom.[45]

https://doi.org/10.1021/acsomega.4c01395
ACS Omega 2024, 9, 21287−21297

The Te Kα XFH of an exfoliated crystal of $Fe_{5-x}GeTe_2$ was measured at 113 and 133 K at BL47XU in SPring-8, i.e., the employed sample is a crystal of $Fe_{5-x}GeTe_2$. The crystal was cooled to the above temperatures using a liquid-nitrogen open-flow cooler. Figure 1a also shows a photograph of the $Fe_{5-x}GeTe_2$ crystal. The incident X-ray energies for XFH data collection were 32.5−35.0 keV in steps of 0.5 keV (6 energies) for both 133 and 113 K; data collection was performed using a CdTe 2D detector. The sample was placed on the two-axis table of the diffractometer. The measurements were performed in an inverse mode by rotating the two axes of the sample stage, at an incident angle of $0° \leq \theta \leq 75°$ in steps of 1.0°, and at an azimuthal angle of $0° \leq \varphi \leq 360°$ in steps of 0.25°. The experimental details of the XFH measurements have been previously described.[46,47]

The XFH data were processed by subtracting the background from the X-ray fluorescence data, and an extension of the XFH data was performed by considering the 3-fold symmetry of $Fe_{5-x}GeTe_2$ based on the space group of $R\bar{3}m$ (no. 166). The atomic image was reconstructed by the Fourier transformation of the XFH data using the multiple-energy Barton's algorithm;[48] the XFH simulation was performed based on the crystal structure of $Fe_{5-x}GeTe_2$. The atomic image that was reconstructed by the Fourier transformation of XFH simulated for the 1 × 1 structure was compared with the experimentally obtained atomic images to perform a detailed analysis of the local structure. In the simulation, the Fourier transformation was performed using Barton's algorithm,[48] similar to when obtaining the atomic image reconstructed from experimental XFH data. The actual Fourier transformation of the experimental and simulated XFH data was performed using 3D-AIR IMAGE software.[49]

RESULTS AND DISCUSSION

Figure 1b shows the crystal structure of $Fe_{5-x}GeTe_2$ that was drawn based on the atomic coordinates previously reported.[36] The space group of this crystal is $R\bar{3}m$ (no. 166), which is defined by a and c through the axis transformation to the trigonal lattice ($a = b \neq c$, $\alpha = \beta = 90°$ and $\gamma = 120°$). All atoms of Te, Ge, and the three types of Fe (Fe1, Fe2, and Fe3) in $Fe_{5-x}GeTe_2$ occupy the 6c site (0,0,z'); $z' = 0.21896$ for Te, $z' = 0.01074$ for Ge, $z' = 0.07305$ for the Fe1 site, $z' = 0.30917$ for the Fe2 site, and $z' = 0.39597$ for the Fe3 site.[36] Here, the Fe1, Fe2, and Fe3 sites are named to distinguish the three Fe atoms, as reported in previous papers.[36,41] The lattice constants, a and c, are 4.06561(9) and 29.443(5) Å, respectively, for this sample.[44] Additionally, the values of a and c are consistent with those reported previously.[36] The stoichiometry is $Fe_{4.5(5)}Ge_{1.02(9)}Te_2$, as established by EDX.[44]

The temperature-dependent K-edge EXAFS spectra of $Fe_{5-x}GeTe_2$ are shown in Figure 2a. The energy of K-edge was constant over the entire temperature range (100−298 K), as seen from the similar EXAFS spectra at all temperatures, implying an invariant valence of the Te atom. The temperature selected for the EXAFS measurement corresponded to each magnetic phase (FM, FM plus CO, and FM plus faded CO). In particular, a temperature below or above T_{C2} was significant because the emergence of the CO state induces the formation of a Te trimer (i.e., Te−Te distance shortening and elongation). As examples, the weighted EXAFS oscillation $k^3\chi(k)$'s of $Fe_{5-x}GeTe_2$ at 298 and 100 K are shown in Figure 2b,c, respectively, where k refers to the wave vector defined from the inflection point of the Te K-edge peak as the criterion.

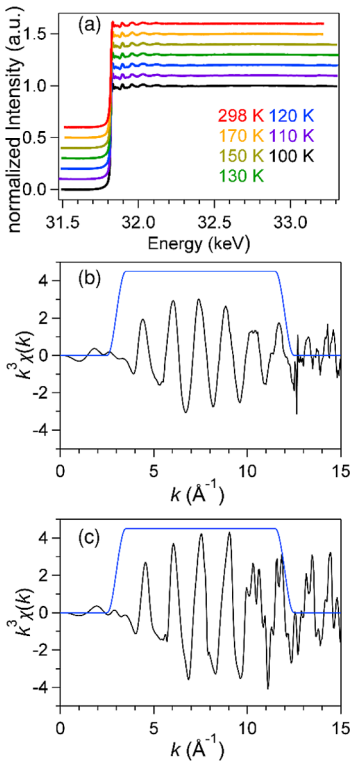

Figure 2. (a) Temperature-dependent Te K-edge EXAFS of $Fe_{5-x}GeTe_2$. $k^3\chi(k)$'s of $Fe_{5-x}GeTe_2$ at (b) 298 K and (c) 100 K.

Figure 3a,b shows the radial distribution functions $\Phi(r)$ obtained via the Fourier transformation of $k^3\chi(k)$ at 298 and 100 K, respectively. A single pronounced peak is obtained in each $\Phi(r)$, which originates from the Te−Fe1, Te−Fe2, and Te−Fe3 scatterings; the predicted distances of Te−Fe1, Te−Fe2, and Te−Fe3 are 2.629, 2.638, and 2.782 Å, respectively, at room temperature.[36] These scatterings could not be resolved in the peak because of apparently a single peak. The fractional occupancy of the Te−Fe1 scattering was 40%, as confirmed by the atomic coordinates reported by May et al.[36] As described later, the weighted average value of the Te−Fe distances ascribable to the above three scatterings was used as the initial value in the parameter fitting for $\chi(k)$ obtained by an inverse-Fourier transformation of the single peak of $\Phi(r)$. The small $\Phi(r)$ peaks assigned to the interlayer and intralayer Te−Te scatterings (3.848 and 4.044 Å), Te−Ge scattering (3.826 and 4.341 Å), and Te−Fe1 scattering (4.267 Å) are observed in an r range of 3−4 Å, as shown in Figure 3a,b.

The $\chi(k)$'s obtained using an inverse-Fourier transformation of the intense single $\Phi(r)$ peaks (r = 1.72−2.75 Å) observed at 298 and 100 K are shown in Figure 3c,d, respectively. For $\chi(k)$, parameter fitting was performed using a general EXAFS formula,[50−52] as described above, and only a single-shell fitting was performed by compiling three scatterings of Te−Fe1, Te−Fe2, and Te−Fe3. The total coordination number around the Te atom was fixed at 5.2 (=3 × 0.4 + 1 + 3, because the coordination numbers of Fe1, Fe2, and Fe3 are 3, 1, and 3, respectively, and the fractional occupancy of Fe1 is 40%, whereas that of Fe2 and Fe3 is 100%. The average distance r_{Te-Fe} related to the single pronounced $\Phi(r)$ peak and the Debye−Waller factor (thermal fluctuation parameter)

https://doi.org/10.1021/acsomega.4c01395
ACS Omega 2024, 9, 21287−21297

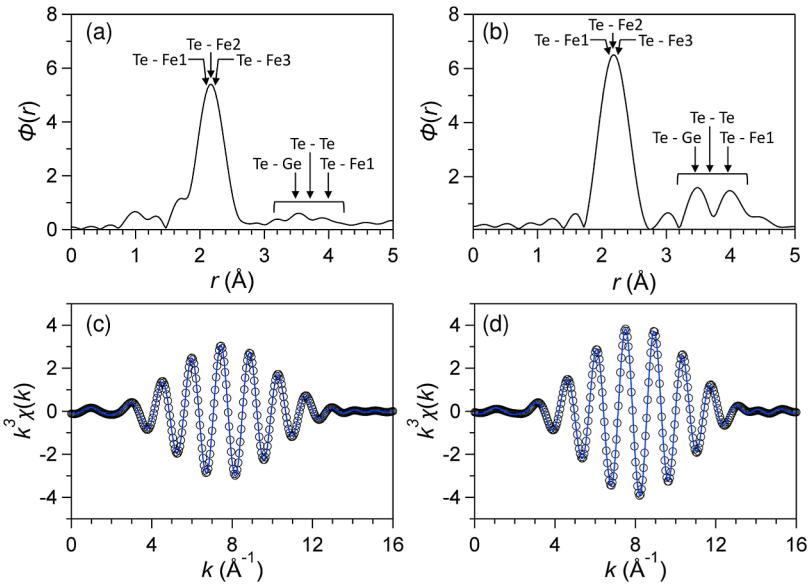

Figure 3. $\Phi(r)$'s of $Fe_{5-x}GeTe_2$ at (a) 298 K and (b) 100 K. The $\Phi(r)$'s are obtained from the Fourier transformation of $k^3\chi(k)$'s in the k-space of 3.0−12 Å for 298 K and 3.0−12 Å for 100 K (see Figure 2). $\chi(k)$'s at (c) 298 K and (d) 100 K obtained from the inverse Fourier transformation of $\Phi(r)$'s at r = 1.75−2.85 Å (see (a) and (b)). Notice that the peak position of $\Phi(r)$ is smaller than the real distance because of phase shift. In (c) and (d), the experimental and calculated $\chi(k)$'s are indicated by black circles and blue lines, respectively. The calculated $\chi(k)$ refers to the best fitted $\chi(k)$ for the experimental one obtained by the least-squares fitting to provide the structural parameters including real distance and the Debye−Waller factor.

$\sigma_{Te-Fe}(2)$ were determined by parameter fitting; $\sigma(2)$ refers to the harmonic thermal displacement factor. Figure 3c,d shows that the $\chi(k)$s calculated using the final parameters that were determined based on the general EXAFS formula reproduce the experimental $\chi(k)$s well, implying that the finally determined r_{Te-Fe} and $\sigma_{Te-Fe}(2)$ are reliable.

The temperature dependence of r_{Te-Fe} and $\sigma_{Te-Fe}(2)$ related to Te−Fe scattering is shown in Figure 4a,b, respectively. The values of r_{Te-Fe} and $\sigma_{Te-Fe}(2)$ decrease as the temperature decreases to 170 K. In fact, more data points may be necessary for the detailed analysis of the variation of r_{Te-Fe} and $\sigma_{Te-Fe}(2)$ in the temperature range of 170−300 K, which is a future task.

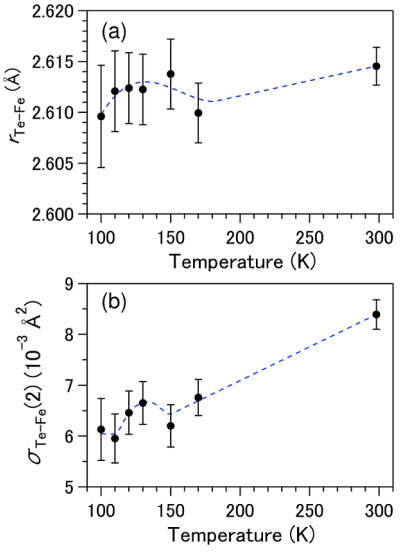

Figure 4. Temperature dependence of (a) r_{Te-Fe} and (b) $\sigma_{Te-Fe}(2)$ relating to Te−Fe scatterings determined from the Te K-edge EXAFS of $Fe_{5-x}GeTe_2$. The thin solid lines refer to the eye guides.

The median value of r_{Te-Fe} increases slightly below 170 K, reflecting the elongation of the Te−Fe distance. Actually, there is a problem that the error bars are a little large (Figure 4a), but the variation of median value of r_{Te-Fe} was well reproduced by some parameter fittings with different initial values and the increase in r_{Te-Fe} was systematically observed at multiple temperature points below 170 K, guaranteeing the reliability of the variation. This temperature is similar to that (T_{C2} = 165 K)[41] of the transition from FM to FM plus CO. This result is also self-consistent with the structure model reported previously (Figure 1c).[36,41,44] The model indicates that the formation of the Te trimer (or the formation of the $(\sqrt{3} \times \sqrt{3})R30^\circ$ superstructure) accompanied by the CO phase transition is caused by the movement of a Te atom toward an Fe1 site unfilled by an Fe atom within the z = 0 Å plane (or Te plane), as seen from Figure 1b,c; the Te atom comes to be far from the Fe1 site filled by an Fe atom within the z = 0 Å plane and increases the Te−Fe1 distance (i.e., to enhance r_{Te-Fe}).

If this is appropriate, the Te−Fe1 distance will always increase during the CO phase transition. However, the elongation observed by EXAFS is too small (∼0.005 Å), despite the expected variation, $\Delta(r)$ of 0.29 Å, of the Te−Fe1 distance produced by the CO transition, where $\Delta(r)$ is calculated by considering the movement of 0.4 Å of a Te atom to the center of the Te trimer, as reported by Eguchi et al.[44] (see Figure 1c), i.e., $\Delta(r) = \frac{1}{2}[r_{Te-Fe1}(1) + r_{Te-Fe1}(2)]$ for $(\sqrt{3} \times \sqrt{3})R30^\circ - r_{Te-Fe1}$ for $(1 \times 1) = \frac{1}{2}(2.998 + 2.837) - 2.63$ Å = 0.29 Å, where a = 4.065 Å[44] and z = 1.2 Å for the Fe1 plane (see Figure 1c). Here, it should be noted that $r_{Te-Fe1}(1)$ and $r_{Te-Fe1}(2)$ refer to two types of Te−Fe1 distances for the $(\sqrt{3} \times \sqrt{3})R30^\circ$

https://doi.org/10.1021/acsomega.4c01395
ACS Omega 2024, 9, 21287−21297

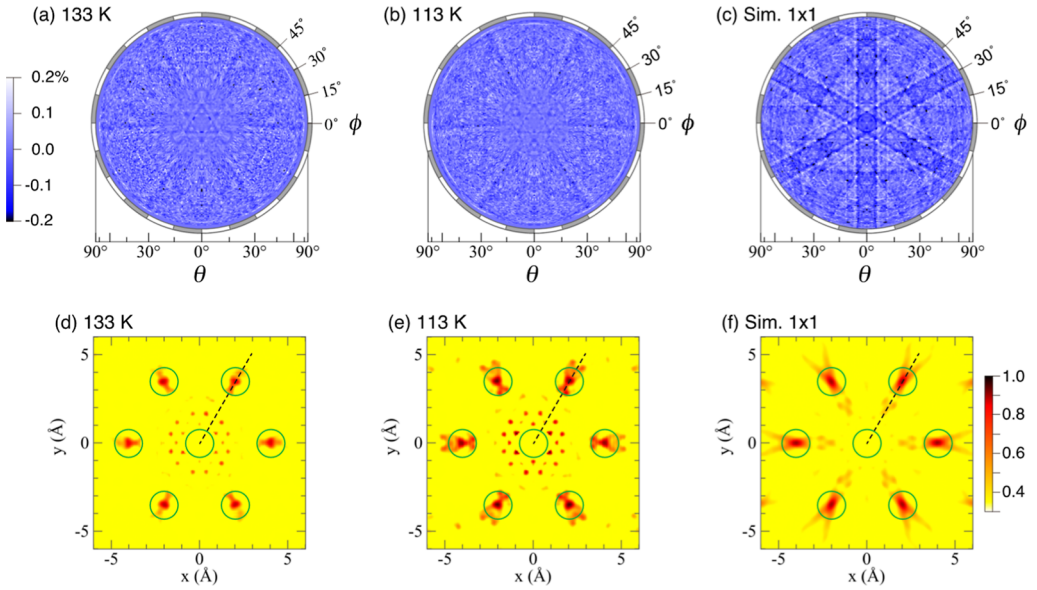

Figure 5. Te Kα XFH of $Fe_{5-x}GeTe_2$ at (a) 133 K and (b) 113 K. (c) Te Kα XFH simulated for the 1 × 1 structure. The atomic coordinates listed in ref 36 are employed for the simulation of XFH. Reconstructed atomic images at z = 0 Å of $Fe_{5-x}GeTe_2$ at (d) 133 K and (e) 113 K, which are obtained by the Fourier transformation of Te Kα XFHs. The green circles indicate the positions of the Te atoms predicted from the crystal structure.[36] The dashed lines in (d) and (e) correspond to the directions for depicting the profile patterns shown in Figure 6a,b. (f) Atomic image reconstructed from the simulated XFH shown in (c).

structure, respectively, while r_{Te-Fe1} refers to the Te−Fe1 distance for the 1 × 1 structure. This fact implies that the Te−Fe2 and Te−Fe3 scatterings are captured in addition to three Te−Fe1 scatterings (Te−Fe1, Te−Fe1(1), and Te−Fe1(2)) in the $\Phi(r)$ peak at 1.75−2.85 Å below 170 K (or below the CO transition temperature), i.e., the single shell fitting prevents the accurate observation of the elongation of the Te−Fe1 distance. In addition, the median value of $\sigma_{Te-Fe}(2)$ decreases monotonically with decreasing temperature to 150 K and increases once the temperature drops below 150 K regardless of a little large error bars, as shown in Figure 4b. This median value was well reproduced through some parameter fittings, and the increase in $\sigma_{Te-Fe}(2)$ is also confirmed at multiple temperature points below 150 K, in the same manner as the case of r_{Te-Fe1}. This occurrence implies that EXAFS captures the thermal fluctuation or static disorder originating from the CO phase transition. This phenomenon based on the frustration in the formation of the Te trimer will be discussed later.

The direct movement of Te, which reflects the shortening or elongation of the Te−Te distance, could not be captured from EXAFS, because of the weak and complex $\Phi(r)$ peaks in the range of 3−4 Å, which are ascribable to Te−Te scatterings (see Figure 3a,b). For direct confirmation of the Te trimer, the Te Kα XFH was measured at 133 and 113 K. Figure 5a,b shows the XFHs at 133 and 113 K, respectively; clear standing wave lines with 6-fold symmetry are visible. Figure 5c shows the Te Kα XFH simulated with only a 1 × 1 crystal structure for comparison. 6-fold standing wave lines are observed, but the finer details are different from those of the experimental XFHs (Figure 5a,b).

The reconstructed atomic images on the *ab* plane at z = 0 Å (or Te plane), which are obtained via a Fourier transformation of the XFHs at 133 and 113 K, are shown in Figure 5d,e, respectively. The reconstructed atomic image directly reflects the *ab* plane containing only Te atoms (Figure 1b,c). Here, it should be noticed that the reconstructed images (Figure 5d,e) provide reliable atomic images that artifacts are very few owing to the z = 0 plane (i.e., the original Te plane), guaranteeing the reasonable discussion on the formation of trimers of Te atoms. As seen from Figure 5d,e, the circles drawn with solid lines indicate the position of a Te atom predicted from the 1 × 1 crystal structure (Figure 1b,c); the radius of the circle is 0.5 Å. The center circle is related to the emitter atom (Te); however, in principle, the atomic image is not observed in XFH. Atomic images are clearly observed in the circles for both the reconstructed planes at 133 and 113 K, indicating that the crystal structure was maintained at both temperatures. In addition, the shapes of the experimental atomic images (Figure 5d,e) are different from those simulated based on the 1 × 1 crystal structure (Figure 5f), indicating the formation of the $(\sqrt{3} \times \sqrt{3})R30°$ structure accompanied by a CO transition, as described below.

Here, we comment on the lack of the reconstructed image obtained from experimental Te Kα XFH at 300 K which should take the 1 × 1 crystal structure. In this study, the XFH measurement at 300 K was not conducted, but we point out that the comparison of experimentally reconstructed atomic images at 113 and 133 K with the simulated one is meaningful because the clear difference was observed to indicate the variation from the 1 × 1 crystal structure. In addition, the atomic image and line profile simulated assuming the crystal phase consists of a 50% $(\sqrt{3} \times \sqrt{3})R30$ structure and a 50% 1 × 1 crystal structure in $Fe_{5-x}GeTe_2$ are shown in Figure S1, which are consistent with the experimental atomic images and line profiles at 113 and 133 K shown in Figures 5 and 6, indicating the reliability of the simulation. The result clearly indicates the partial formation of $(\sqrt{3} \times \sqrt{3})R30$ structures at low temperature. In other words, the simulation well reproduces the experimental atomic images and line profiles at 113 and 133 K. Therefore, the observation of experimental Te Kα XFH at 300 K is a future important task, but the atomic image simulated for the 1 × 1 structure (see Figure 5f) should

https://doi.org/10.1021/acsomega.4c01395
ACS Omega 2024, 9, 21287−21297

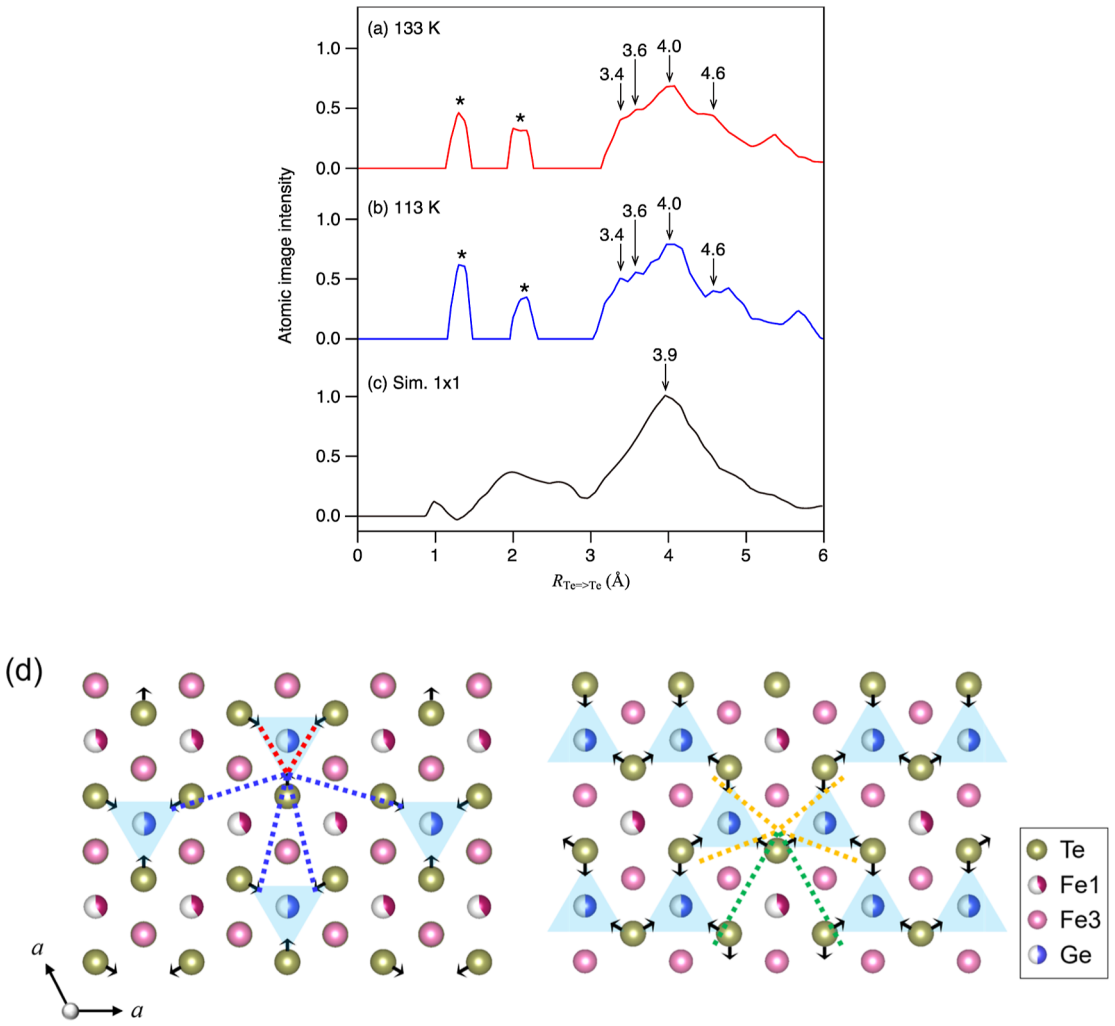

Figure 6. Line profiles of atomic images along the dashed lines (Figure 5d,e) from the center toward the Te atom at z = 0 Å reconstructed from Te Kα XFH of $Fe_{3-x}GeTe_2$ at (a) 133 K and (b) 113 K; $R_{Te\Rightarrow Te}$ refers to the distance from the center along the dashed line. The numerical values shown in the line profiles refer to the corresponding values of $R_{Te\Rightarrow Te}$ (Å). The peaks labeled with asterisks correspond to ghost peaks (or artifacts) produced by the Fourier transformation in the limited wave vector range. (c) The simulated line profile of the 1 × 1 structure along the same direction as (a) and (b). The simulation was conducted using the atomic coordinates listed in ref 36. (d) Schematic representation of the formation of $(\sqrt{3} \times \sqrt{3})R30^\circ$ superstructures, in which two layers constitute the asymmetry unit. In (c), the red/yellow dashed and blue/green dashed lines refer to the shortened Te−Te and elongated Te−Te distances, respectively, that are produced by the CO transition. The predicted values are 3.37 Å (red) and 3.77 Å (yellow) for the shortened Te−Te and 4.45 Å (blue) and 4.59 Å (green) for the elongated Te−Te.

possess the reliability enough to discuss structural variation between 300 and 113 K/133 K. The partial formation of the $(\sqrt{3} \times \sqrt{3})R30$ structure at 113 and 133 K is fully discussed later.

The atomic images at 133 and 113 K show an ellipsoidal shape with the long axis directed toward the center (Te atom), as shown in Figure 5d,e, suggesting a static displacement or a dynamic displacement (i.e., thermal fluctuation) of the Te atom. A similar ellipsoidal atomic image was also observed in the Te plane, which was reconstructed from the Ge Kα XFH at 298, 175, and 123 K.[44] The Te atom fluctuated exactly along the direction toward the center. Multiple atomic spots were found in the ellipsoidal atomic images at 133 and 113 K (Figure 5d,e), whereas only a single spot was observed in the ellipsoidal image simulated with a 1 × 1 structure (Figure 5f).

Moreover, the atomic image of Te becomes more intense at 113 K, and part of the atomic image protrudes from the circle extending along the direction toward the center (see Figure 5e). This result is reasonable because thermal fluctuations would be suppressed by cooling the sample. The ellipsoidal extension and multiple spots observed in the atomic images of Te at 133 and 113 K may have originated from the formation of trimers of Te atoms caused by the CO transition. In this instance, XFH directly captures the movement of the Te atom at low temperatures. Furthermore, the elongation of r_{Te-Fe1} below 170 K observed in EXAFS would be closely associated with the extension of the atomic image observed in XFH.

The atomic image of the Te plane at z = 3.3 Å was reconstructed from Ge Kα XFH at 123 K, which was obtained in the previous study,[44] and it corresponds directly to the Te plane at z = 0 Å, which was obtained from Te Kα XFH in this study. The atomic image reconstructed from Ge Kα XFH at 123 K also shows the splitting of the atomic spot, reflecting the partial formation of the Te trimer.[44] Thus, a clear splitting is indicated in the line profile at 123 K, as reported by Eguchi et al.[44] In this study, we also depicted the line profile along the dashed line (i.e., Te−Te direction), as shown in Figure 5d,e (see Figure 6a,b), providing the three splitting peaks at both

https://doi.org/10.1021/acsomega.4c01395
ACS Omega 2024, 9, 21287−21297

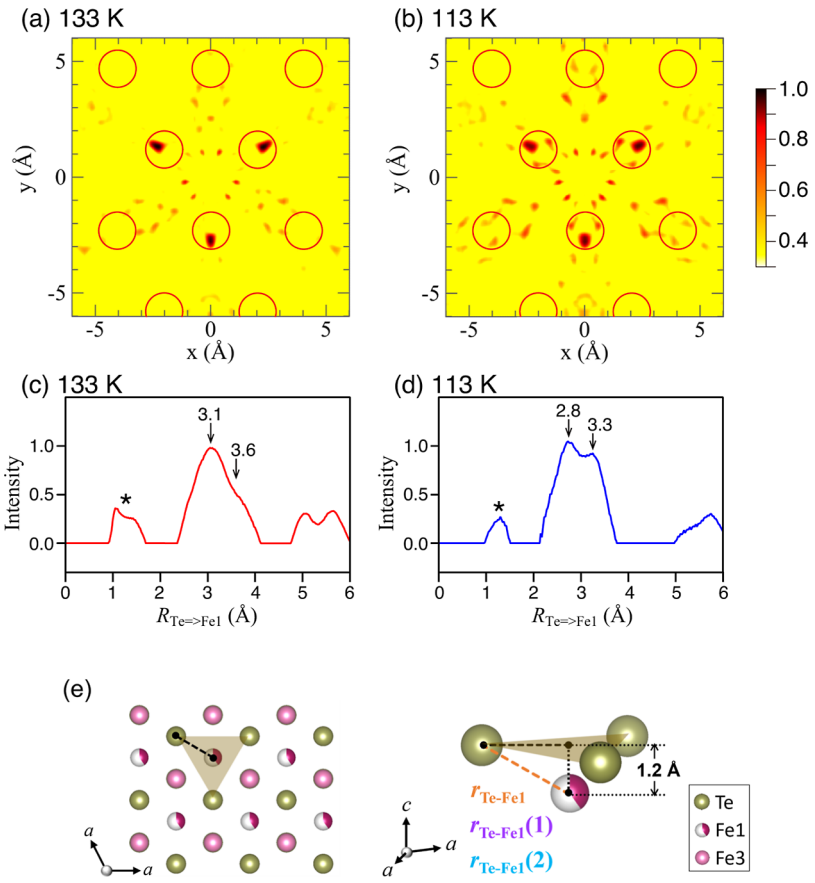

Figure 7. Reconstructed atomic images at z = 1.2 Å of $Fe_{5-x}GeTe_2$ at (a) 133 K and (b) 113 K, which were obtained by the Fourier transformation of Te Kα XFHs. The red circles indicate the positions of the Fe1 sites, as predicted from the crystal structure.[36] Line profiles along the lines of Te (z = 0 Å)−Fe1 (z = 1.2 Å) of $Fe_{5-x}GeTe_2$ at (c) 133 K and (d) 113 K. The numerical values shown in the line profiles refer to the corresponding values of $R_{Te⇒Fe1}$ (Å). The peak marked with an asterisk corresponds to a ghost peak (or artifact) produced by the Fourier transformation in the limited wave vector range. (e) Schematic representation of the Te−Fe1 distance in the 1 × 1 and $(\sqrt{3} \times \sqrt{3})R30°$ structures. The length of the Te−Fe1 distance ($R_{Te⇒Fe1}$) is indicated by an orange line, which encompasses r_{Te-Fe1} for 1 × 1 and $r_{Te-Fe1}(1)$ and $r_{Te-Fe1}(2)$ for $(\sqrt{3} \times \sqrt{3})R30°$ (see (e)).

temperatures; the peak splitting implies the shortening of the Te−Te distance ($(\sqrt{3} \times \sqrt{3})R30°$ superstructure), the consistence of the Te−Te distance (1 × 1 structure), and the elongation of the Te−Te distance ($(\sqrt{3} \times \sqrt{3})R30°$ superstructure), which are caused by the partial formation of the CO state. The simulated line profile for the 1 × 1 structure is shown in Figure 1c, providing a single broad peak with a center position of 3.9 Å.

The Te−Te distances were established to be 3.4, 3.6, 4.0, and 4.6 Å at 133 K from the four-way splitting of the line profile at 133 K (Figure 6a). The values are consistent with those obtained from the crystal structure,[36] STEM,[36] and STM,[40,41] as well as Ge Kα XF;[44] the Te−Te distances are 3.37 and 3.77 Å for the short Te−Te, 4.07 Å for Te−Te in the 1 × 1 structure, and 4.45 and 4.59 Å for the elongation of Te−Te. The Te−Te distances are schematically shown in Figure 6d. Admittedly, the profile peak at 113 K is very similar to that at 133 K; however, the peak splitting is clearer owing to the suppression of the thermal fluctuation.

Here, we must comment on the proportions of $(\sqrt{3} \times \sqrt{3})R30°$ and 1 × 1, which are present; the XFH results are used to determine the fraction. The line profiles at 133 and 113 K (Figure 6a,b) indicate the existence of both structures; 50% $(\sqrt{3} \times \sqrt{3})R30°$ and 50% 1 × 1 structures are suggested from the simulation (see Figure S1). A previous study of Ge Kα XFH of $Fe_{5-x}GeTe_2$ reported an equivalent (50%) proportion for each structure; this conclusion was reached because the line profile displayed two split peaks of the same intensity, which were ascribable to the $(\sqrt{3} \times \sqrt{3})R30°$ and 1 × 1 structures.[44] If the Fe atom completely occupies the Fe1 site, the $(\sqrt{3} \times \sqrt{3})R30°$ structure is present in 100% proportion because a completely ordered structure is produced, as shown in Figure 1c. However, a 40% occupancy of Fe atoms at the Fe1 site, exactly 43.7(8)% occupancy as described in ref 36, produces disorder in the crystal lattice to suppress the formation of the $(\sqrt{3} \times \sqrt{3})R30°$ structure, which should result in the partial formation of $(\sqrt{3} \times \sqrt{3})R30°$ and 1 × 1 structures; this scenario is consistent with that observed from the experimental results (Figure 6a,b) and that observed by Eguchi et al.[44] Moreover, we can comment on the presence of completely occupied/ordered area indispensable for the formation of trimers of Te atoms. Namely, the occupied/ordered area of Fe1 must spread with a certain size into the crystal, indicating that 40% occupied Fe atoms at the Fe1 site implies the formation of the ordered area which is phase-separated from the defect area (nonoccupied area). More strictly speaking, the ordered area

https://doi.org/10.1021/acsomega.4c01395
ACS Omega 2024, 9, 21287−21297

producing the $(\sqrt{3} \times \sqrt{3})R30$ charge ordered state exists as island into the defect area.

As shown in Figure 6d, the Te atoms approach the center of the Te trimer, underneath which the Ge atom occupied (i.e., the Fe atom does not occupy the Fe1 site). On the left side of Figure 6d, it is evident that the Te atom moves in one direction, whereas on the right side of Figure 6d, the Te atom moves in two directions, and the latter causes frustration. The resultant frustration produces fluctuations in the Te atom. Thus, the enhancement in $\sigma_{Te-Fe1(2)}$ below 150 K presumably reflects the fluctuation of the Te atom, as shown on the right side of Figure 6d. In other words, EXAFS captures the structural frustration that accompanies the CO phase transition.

The previously reported Ge Kα XFH provided clear reconstructed atomic images in the Te and Ge planes and the Fe2/Fe3 planes, as predicted from the crystal structure (Figure 1b); however, the atomic image of the Fe atom in the Fe1 site was ambiguous.[44] This ambiguity could be due to the low occupancy of Ge (50%) and Fe atoms at the Fe1 site (40%). By contrast, in this study, the Te Kα XFH provided clear atomic images in the Fe1 site (z = 1.2 Å) (Figure 7a,b), owing to the complete occupation of the Te atom despite the fractional occupancy (40%) of the Fe atom at the Fe1 site.

From Figure 7a,b, it is apparent that the three circles (Fe1 sites) near the center are occupied by Fe atoms. The atomic image at the Fe1 site deviates in the outer direction, indicating that the Fe atom tends to move away from the Te atom; this occurrence is consistent with the elongation of Te−Fe distance observed below 170 K indicated by EXAFS (Figure 4a). As seen from the schematic representation of the CO $(\sqrt{3} \times \sqrt{3})R30°$ superstructure shown in Figures 1c and 6d, the Te atoms always move away from the Fe atom at the Fe1 site during the formation of the $(\sqrt{3} \times \sqrt{3})R30°$ superstructure, which should shift the atomic spot outward.

The line profile along the Te (z = 0 Å)−Fe1 (z = 1.2 Å) line at 133 and 113 K is shown in Figure 7c,d, respectively. A broad Te−Fe1 atomic peak is observed at ∼3.1 Å. The central peak at 133 K is located at a value higher than that of r_{Te-Fe1} = 2.63 Å for the 1 × 1 structure and is almost consistent with $r_{Te-Fe1}(1)$ = 2.84 Å and $r_{Te-Fe1}(2)$ = 3.00 Å for the $(\sqrt{3} \times \sqrt{3})R30°$ superstructure predicted from the crystal structure.[36,40,41,44] The broad line profile reflects all the Te−Fe1 distances originating in the $(\sqrt{3} \times \sqrt{3})R30°$ superstructure and the 1 × 1 structure. A schematic representation of the Te−Fe1 distance is shown in Figure 7e.

Moreover, the line profile (Figure 7c) shows a shoulder at 3.6 Å. Upon considering the Te−Fe1 distance that is next longer, $r_{Te-Fe1}(3)$, to explain the line profile, we discovered it was too long (∼4.53 or ∼4.66 Å). This result implies that the Te atom moves to the center of the Te trimer within the z = 0 plane owing to the formation of the $(\sqrt{3} \times \sqrt{3})R30°$ structure and that the Fe atom at the Fe1 site may simultaneously move outward, thus resulting in a longer Te−Fe1 distance. Hence, the broad atomic profile pattern may reflect the influence of the movement of Fe atoms at the Fe1 site, in addition to Te movement. Direct evidence of the movement of Fe atoms at the Fe1 sites was not obtained in this study. The broad atomic peak observed at 133 K splits into two broad peaks at 113 K centered at 2.8 and 3.3 Å, because the thermal fluctuation is suppressed, as indicated by the line profile of the Te atom shown in Figure 6b. The origin of the peak located at 3.3 Å at 113 K is still unclear, and we will be investigating the movement of the Fe1 atom.

Of particular note, the atomic image of the Fe atom is similar at 133 and 113 K (Figure 7a,b), i.e., the position of the Fe atom does not shift when the temperature decreases from 133 to 113 K; however, the line profile is more split at 113 K (see Figure 7c,d). Moreover, at 133 K, trimer formation of Te atoms is well underway. The thermal displacement is suppressed by decreasing the temperature, and clearer atomic images are obtained.

The atomic images reconstructed at z = 1.5 Å, z = 2.6 Å, z = 3.0 Å, and z = 3.6 Å are shown in Figure 8a−d, respectively;

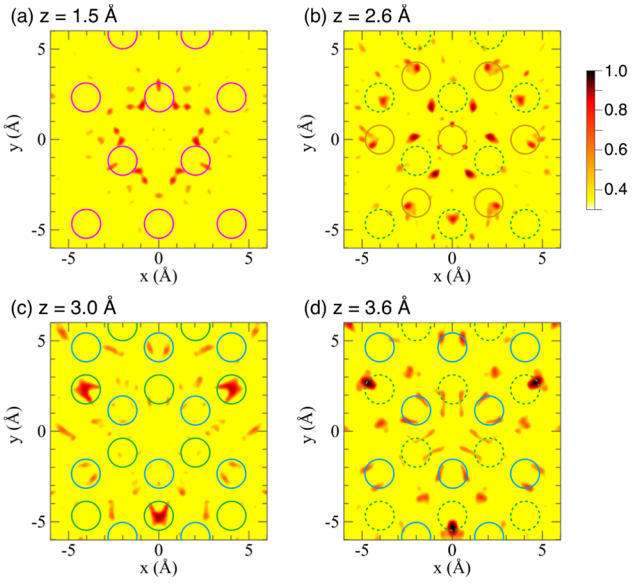

Figure 8. Reconstructed atomic images at z = (a) 1.5 Å, (b) 2.6 Å, (c) 3.0 Å, and (d) 3.6 Å of $Fe_{5-x}GeTe_2$ at 113 K, which were obtained by the Fourier transformation of Te Kα XFHs. The circles drawn in orange, pink, blue, and green indicate Fe2, Fe3, Ge, and Te, respectively. The solid and dashed circles indicate atoms within and near the z plane, respectively, i.e., the dashed circle deviates slightly from the z plane. All circles are drawn based on the atomic coordinates listed in ref 36.

they can be assigned to the planes of Fe3, Fe2, and Ge/Te; Ge atoms are located in two different planes and have an occupancy of 50% at z = 3.0 Å, and z = 3.6 Å. The atomic image of Fe3 shown in Figure 8a seems to be located toward the outermost position of the circle, as predicted from the crystal structure.[36,40,41,44] This may be attributed to the fact that the elongated Te−Fe3 shown in the left of Figure 6d contributes strongly to the XFH, in contrast to that of the shortened Te−Fe3 (left of Figure 6d) and that of the elongated/shortened Te−Fe3 (right of Figure 6d). That is, the elongated Te−Fe3 produces an elliptical atomic image along the outer direction. The weak contribution of the Te−Fe3 scattering, other than that of the elongated Te−Fe3 on the left side of Figure 6d, originates from the movement of the Te atom in two different directions. However, the origin must be more carefully discussed owing to the weak intensity of atomic images and presence of artifacts (Figure 8a). Actually, the artifacts caused by the truncation effect in Fourier transformation of XFH data were not confirmed in the all reconstructed images shown in Figure 8, because of no observation of sidelobes which emerge by the truncation of

https://doi.org/10.1021/acsomega.4c01395
ACS Omega 2024, 9, 21287−21297

Fourier transformation.[53] Namely, more complex and intrinsic effect producing the artifacts observed outside circles (Figure 8) may exist such as such as conjugate images.

An atomic image of Fe2 is also observed in the outermost position of the circle (Figure 8b) and may be ascribed to similar factors as those elucidated above for Fe3. Moreover, the weak Ge and intense Te images (Figure 8c,d) are due to the occupancy of Te and Ge (100% for Te and 50% for Ge) and the difference in their atomic numbers. The discussion regarding the atomic images at z = 3.0 and 3.6 Å may be ambiguous owing to the distance far from the original emitter Te atom. To sum up, the discussion of atomic location based on the reconstructed images (Figure 8) must be performed in more prudent manner, owing to the weak atomic spots, as well as presence of artifacts.

CONCLUSIONS

The Te K-edge EXAFS and Te Kα XFH of $Fe_{5-x}GeTe_2$ successfully captured the formation of the trimer of Te atoms (or the formation of a $\sqrt{3} \times \sqrt{3}$ superstructure) at 133 and 113 K. The proportion of the $\sqrt{3} \times \sqrt{3}$ superstructure was 50% and is consistent with that obtained previously from Ge Kα XFH.[34] Thus, in this study, the Te K-edge EXAFS and Te Kα XFH directly clarified the local structure around the Te atom at low temperature. Moreover, the atomic image at the Fe1 site, which was not observed in the Ge Kα XFH, was first detected in the Te Kα XFH. The atomic image produced was dependent on the movement of the Te atom, i.e., the Fe atom at the Fe1 site moved outward. This occurrence can be explained by the fact that the Fe atom located at the Fe1 site moved away from the Te atom during the CO transition (or the formation of the $\sqrt{3} \times \sqrt{3}$ superstructure and Te trimer). Throughout this study, the structural variation accompanying the transition from FM to FM and CO-ordered states was thoroughly investigated and reasonably understood.

ASSOCIATED CONTENT

Supporting Information

The Supporting Information is available free of charge at https://pubs.acs.org/doi/10.1021/acsomega.4c01395.

Atomic image and line profile for the original Te plane (z = 0 Å) simulated assuming the crystal phase consisting of a 50% charge-ordered $(\sqrt{3} \times \sqrt{3})R30^\circ$ superstructure and a 50% 1 × 1 structure of $Fe_{5-x}GeTe_2$, and the line profile simulated for a single phase of the 1 × 1 structure of $Fe_{5-x}GeTe_2$ (PDF)

AUTHOR INFORMATION

Corresponding Author

Yoshihiro Kubozono − *Research Institute for Interdisciplinary Science, Okayama University, Okayama 700-8530, Japan;* orcid.org/0000-0002-7910-0308; Email: kubozono@cc.okayama-u.ac.jp

Authors

Ritsuko Eguchi − *Research Institute for Interdisciplinary Science, Okayama University, Okayama 700-8530, Japan;* orcid.org/0000-0003-3263-5935

Halubai Sekhar − *Department of Physical Science and Technology, Nagoya Institute of Technology, Nagoya 466-8585, Japan*

Koji Kimura − *Department of Physical Science and Technology, Nagoya Institute of Technology, Nagoya 466-8585, Japan; Research Center for Advanced Measurement and Characterization, National Institute for Materials Science, Tsukuba, Ibaraki 305-0047, Japan; Japan Synchrotron Radiation Research Institute (JASRI), Sayo, Hyogo 679-5198, Japan;* orcid.org/0000-0001-5485-3672

Hirokazu Masai − *Department of Materials and Chemistry, National Institute of Advanced Industrial Science and Technology (AIST), Osaka 563-8577, Japan;* orcid.org/0000-0003-2310-733X

Naohisa Happo − *Graduate School of Information Sciences, Hiroshima City University, Hiroshima 731-3194, Japan*

Mitsuki Ikeda − *Research Institute for Interdisciplinary Science, Okayama University, Okayama 700-8530, Japan;* orcid.org/0000-0002-3479-8618

Yuki Yamamoto − *Research Institute for Interdisciplinary Science, Okayama University, Okayama 700-8530, Japan*

Masaki Utsumi − *Research Institute for Interdisciplinary Science, Okayama University, Okayama 700-8530, Japan*

Hidenori Goto − *Research Institute for Interdisciplinary Science, Okayama University, Okayama 700-8530, Japan*

Yasuhiro Takabayashi − *Department of Physical Science and Technology, Nagoya Institute of Technology, Nagoya 466-8585, Japan*

Hiroo Tajiri − *Japan Synchrotron Radiation Research Institute (JASRI), Sayo, Hyogo 679-5198, Japan*

Koichi Hayashi − *Department of Physical Science and Technology, Nagoya Institute of Technology, Nagoya 466-8585, Japan; Japan Synchrotron Radiation Research Institute (JASRI), Sayo, Hyogo 679-5198, Japan*

Complete contact information is available at: https://pubs.acs.org/10.1021/acsomega.4c01395

Author Contributions

RE and YK supervised the study. MI prepared and characterized the samples of $Fe_{5-x}GeTe_2$ under discussion with RE, HG, and YK. RE, HS, KK, NH, MI, YY, TU, HT, KH, and YK measured Te Kα XFH. KK, HM, and YK measured the Te K-edge EXAFS. XFH data analyses of XFH were performed by RE, KK, NH, and KH, and EXAFS analysis was performed by RE, HM, YT, and YK. The manuscript was prepared by RE and YK with discussions with KK, HM, NH, HG, KH, and YT. All authors approved the final version of the manuscript.

Notes

The authors declare no competing financial interest.

ACKNOWLEDGMENTS

The authors appreciate Dr. Hironori Ofuchi and Dr. Tetsuo Honma of BL14B2 of SPring-8 for their assitance to measurement of EXAFS. This work was partially supported by JSPS Grants-in-Aid for Transformative Research Areas (A) "Hyper-Ordered Structures Sciences" via Grant numbers, 20H05878, 20H05879, 20H05881, and 20H05882 as well as the Grant from the Okayama Foundation for Science and Technology. Measurements of XFH and EXAFS were performed at 2022B1350 and 2022B1063/2023A1814 of SPring-8, respectively.

REFERENCES

(1) Chhowalla, M.; Shin, H. S.; Eda, G.; Li, L.-J.; Loh, K. P.; Zhang, H. The chemistry of two-dimensional layered transition metal dichalcogenide nanosheets. *Nat. Chem.* **2013**, *5*, 263−275.

(2) Tan, C.; Cao, X.; Wu, X.-J.; He, Q.; Yang, J.; Zhang, X.; Chen, J.; Zhao, W.; Han, S.; Nam, G.-H.; Sindoro, M.; Zhang, H. Recent advances in ultrathin two-dimensional nanomaterials. *Chem. Rev.* **2017**, *117*, 6225−6331.

(3) Hsu, F.-C.; Luo, J.-Y.; Yeh, K.-W.; Chen, T.-K.; Huang, T.-W.; Wu, P. M.; Lee, Y.-C.; Huang, Y.-L.; Chu, Y.-Y.; Yan, D.-C.; Wu, M.-K. Superconductivity in the PbO-type structure α-FeSe. *Proc. Natl. Acad. Sci. U.S.A.* **2008**, *105*, 14262−14264.

(4) Lv, R.; Robinson, J. A.; Schaak, R. E.; Sun, D.; Sun, Y.; Mallouk, T. E.; Terrones, M. Transition metal dichalcogenides and beyond: synthesis, properties, and applications of single- and few-layer nanosheets. *Acc. Chem. Res.* **2015**, *48*, 56−64.

(5) Izumi, M.; Zheng, L.; Sakai, Y.; Goto, H.; Sakata, M.; Nakamoto, Y.; Nguyen, H. L. T.; Kagayama, T.; Shimizu, K.; Araki, S.; Kobayashi, T. C.; Kambe, T.; Gu, D.; Guo, J.; Liu, J.; Li, Y.; Sun, L.; Prassides, K.; et al. Emergence of double-dome superconductivity in ammoniated metal-doped FeSe. *Sci. Rep.* **2015**, *5*, 9477.

(6) Ren, Z.-A.; Lu, W.; Jie, Y.; Yang, J.; Yi, W.; Shen, X.-L.; Li, Z.-C.; Che, G.-C.; Dong, X.-L.; Sun, L.-L.; Zhou, F.; Zhao, Z.-X. Superconductivity at 55 K in iron-based F-doped layered quaternary compound Sm[$O_{1-x}F_x$]FeAs. *Chin. Phys. Lett.* **2008**, *25*, 2215−2216.

(7) Shahi, P.; Sun, J. P.; Wang, S. H.; Jiao, Y. Y.; Chen, K. Y.; Sun, S. S.; Lei, H. C.; Uwatoko, Y.; Wang, B. S.; Cheng, J. G. High-T_c superconductivity up to 55 K under high pressure in the heavily electron doped $Li_x(NH_3)_yFe_2Se_2$ single crystal. *Phys. Rev. B* **2018**, *97*, No. 020508(R).

(8) Ge, J.-F.; Liu, Z.-L.; Liu, C.; Gao, C.-L.; Qian, D.; Xue, Q.-K.; Liu, Y.; Jia, J.-F. Superconductivity above 100 K in single-layer FeSe films on doped $SrTiO_3$. *Nat. Mater.* **2015**, *14*, 285−289.

(9) Zhang, H.; Liu, C.-X.; Qi, X.-L.; Dai, X.; Fang, Z.; Zhang, S.-C. Topological insulators in Bi_2Se_3, Bi_2Te_3 and Sb_2Te_3 with a single Dirac cone on the surface. *Nat. Phys.* **2009**, *5*, 438−442.

(10) Hasan, M. Z.; Kane, C. L. Colloquium: topological insulators. *Rev. Mod. Phys.* **2010**, *82*, 3045−3067.

(11) Ren, Z.; Taskin, A. A.; Sasaki, S.; Segawa, K.; Ando, Y. Optimizing $Bi_{2-x}Sb_xTe_{3-y}Se_y$ solid solutions to approach the intrinsic topological insulator regime. *Phys. Rev. B: Condens. Matter Mater. Phys.* **2011**, *84*, 165311.

(12) Arakane, T.; Sato, T.; Souma, S.; Kosaka, K.; Nakayama, K.; Komatsu, M.; Takahashi, T.; Ren, Z.; Segawa, K.; Ando, Y. Tunable Dirac cone in the topological insulator $Bi_{2-x}Sb_xTe_{3-y}Se_y$. *Nat. Commun.* **2012**, *3*, 636.

(13) Hor, Y. S.; Williams, A. J.; Checkelsky, J. G.; Roushan, P.; Seo, J.; Xu, Q.; Zandbergen, H. W.; Yazdani, A.; Ong, N. P.; Cava, R. J. Superconductivity in $Cu_xBi_2Se_3$ and its implications for pairing in the undoped topological insulator. *Phys. Rev. Lett.* **2010**, *104*, 057001.

(14) Liu, Z.; Yao, X.; Shao, J.; Zuo, M.; Pi, L.; Tan, S.; Zhang, C.; Zhang, Y. Superconductivity with topological surface state in $Sr_xBi_2Se_3$. *J. Am. Chem. Soc.* **2015**, *137*, 10512−10515.

(15) He, T.; Yang, X.; Terao, T.; Uchiyama, T.; Ueno, T.; Kobayashi, K.; Akimitsu, J.; Miyazaki, T.; Nishioka, T.; Kimura, K.; Hayashi, K.; Happo, N.; Yamaoka, H.; Ishii, H.; Liao, Y.-F.; Ota, H.; Goto, H.; Kubozono, Y. Pressure-induced superconductivity in $Ag_{1-x}Bi_{2-x}Se_3$. *Phys. Rev. B* **2018**, *97*, 104503.

(16) Zyuzin, A. A.; Burkov, A. A. Topological response in Weyl semimetals and the chiral anomaly. *Phys. Rev. B: Condens. Matter Mater. Phys.* **2012**, *86*, 115133.

(17) Liu, C.-X.; Ye, P.; Qi, X.-L. Chiral gauge field and axial anomaly in a Weyl semimetal. *Phys. Rev. B: Condens. Matter Mater. Phys.* **2013**, *87*, 235306.

(18) Zhang, K.; Yan, M.; Zhang, H.; Huang, H.; Arita, M.; Sun, Z.; Duan, W.; Wu, Y.; Zhou, S. Experimental evidence for type-II Dirac semimetal in $PtSe_2$. *Phys. Rev. B* **2017**, *96*, 125102.

(19) Xiao, R. C.; Gong, P. L.; Wu, Q. S.; Lu, W. J.; Wei, M. J.; Li, J. Y.; Lv, H. Y.; Luo, X.; Tong, P.; Zhu, X. B.; Sun, Y. P. Manipulation of type-I and type-II Dirac points in PdTe2 superconductor by external pressure. *Phys. Rev. B* **2017**, *96*, 075101.

(20) Soluyanov, A. A.; Gresch, D.; Wang, Z.; Wu, Q. S.; Troyer, M.; Dai, X.; Bernevig, B. A. Type-II Weyl semimetals. *Nature* **2015**, *527*, 495−498.

(21) Deng, K.; Wan, G.; Deng, P.; Zhang, K.; Ding, S.; Wang, E.; Yan, M.; Huang, H.; Zhang, H.; Xu, Z.; Denlinger, J.; Fedorov, A.; Yang, H.; Duan, W.; Yao, H.; Wu, Y.; Fan, S.; Zhang, H.; Chen, X.; et al. Experimental observation of topological Fermi arcs in type-II Weyl semimetal $MoTe_2$. *Nat. Phys.* **2016**, *12*, 1105−1110.

(22) Oritz, B. R.; Gomes, L. C.; Morey, J. R.; Winiarski, M.; Bordelon, M.; Mangum, J. S.; Oswald, I. W. H.; Rodrigiez-Rivera, J. A.; Neilson, J. R.; Wilson, S. D.; Ertekin, E.; McQueen, T. M.; Toberer, E. S. New kagome prototype materials: discovery of KV3Sb5,RbV3Sb5, and CsV3Sb5. *Phys. Rev. Lett.* **2019**, *3*, 094407.

(23) Ortiz, B. R.; Sarte, P. M.; Kenney, E. M.; Graf, M. J.; Teicher, S. M. L.; Seshadri, R.; Wilson, S. D. Superconductivity in the Z2 Kagome metal KV_3Sb_5. *Phys. Rev. Lett.* **2021**, *5*, 034801.

(24) Ortiz, B. R.; Teicher, S. M. L.; Hu, Y.; Zuo, J. L.; Sarte, P. M.; Schueller, E. C.; Abeykoon, A. M. M.; Krogstad, M. J.; Rosenkranz, S.; Osborn, R.; Seshadri, R.; Balents, L.; He, J.; Wilson, S. D. CsV_3Sb_5: A Z_2 topological Kagome metal with a superconducting ground state. *Phys. Rev. Lett.* **2020**, *125*, 247002.

(25) Burch, K. S.; Mandrus, D.; Park, J.-G. Magnetism in two-dimensional van der Waals materials. *Nature* **2018**, *563*, 47−52.

(26) Carteaux, V.; Brunet, D.; Ouvrard, G.; Andre, G. Crystallographic, magnetic and electronic structures of a new layered ferromagnetic compound $Cr_2Ge_2Te_6$. *J. Phys.: Condens. Matter* **1995**, *7*, 69−87.

(27) Gong, C.; Li, L.; Li, Z.; Ji, H.; Stern, A.; Xia, Y.; Cao, T.; Bao, W.; Wang, C.; Wang, Y.; Qiu, Z. Q.; Cava, R. J.; Louie, S. G.; Xia, J.; Zhang, X. Discovery of intrinsic ferromagnetism in two-dimensional van der Waals crystals. *Nature* **2017**, *546*, 265−269.

(28) Li, H.; Ruan, S.; Zeng, Y.-J. Intrinsic van der Waals magnetic materials from bulk to the 2D limit: new frontiers of spintronics. *Adv. Mater.* **2019**, *31*, 1900065.

(29) Huang, B.; Clark, G.; Navarro-Moratalla, E.; Klein, D. R.; Cheng, R.; Seyler, K. L.; Zhong, D.; Schmidgall, E.; McGuire, M. A.; Cobden, D. H.; Yao, W.; Xiao, D.; Jarillo-Herrero, P.; Xu, X. Layer dependent ferromagnetism in a van der Waals crystal down to the monolayer limit. *Nature* **2017**, *546*, 270−273.

(30) McGuire, M. A.; Dixit, H.; Cooper, V. R.; Sales, B. C. Coupling of crystal structure and magnetism in the layered, ferromagnetic insulator CrI_3. *Chem. Mater.* **2015**, *27*, 612−620.

(31) Fei, Z.; Huang, B.; Malinowski, P.; Wang, W.; Song, T.; Sanchez, J.; Yao, W.; Xiao, D.; Zhu, X.; May, A. F.; Wu, W.; Cobden, D. H.; Chu, J.-H.; Xu, X. Two-dimensional itinerant ferromagnetism in atomically thin Fe_3GeTe_2. *Nat. Mater.* **2018**, *17*, 778−782.

(32) Verchenko, V. Y.; Tsirlin, A. A.; Sobolev, A. V.; Presniakov, I. A.; Shevelkov, A. V. Ferromagnetic order, strong magnetocrystalline anisotropy, and magnetocaloric effect in the layered telluride $Fe_{3-\delta}GeTe_2$. *Inorg. Chem.* **2015**, *54*, 8598−8607.

(33) Seo, J.; Kim, D. Y.; An, E. S.; Kim, K.; Kim, G.-Y.; Hwang, S.-Y.; Kim, D. W.; Jang, B. G.; Kim, H.; Eom, G.; Seo, S. Y.; Stania, R.; Muntwiler, M.; Lee, J.; Watanabe, K.; Taniguchi, T.; Jo, Y. J.; Lee, J.; Min, B. I.; Jo, M. H.; Yeom, H. W.; Choi, S.-Y.; Shim, J. H.; Kim, J. S. Nearly room temperature ferromagnetism in a magnetic metal-rich van der Waals metal. *Sci. Adv.* **2020**, *6*, No. eaay8912.

(34) Mondal, S.; Khan, N.; Mishra, S. M.; Satpati, B.; Mandal, P. Critical behavior in the van der Waals itinerant ferromagnet Fe_4GeTe_2. *Phys. Rev. B* **2021**, *104*, 094405.

(35) Stahl, J.; Shlaen, E.; Johrendt, D. The van der Waals ferromagnets $Fe_{5-\delta}GeTe_2$ and $Fe_{5-\delta-x}Ni_xGeTe_2$-crystal structure, stacking faults, and magnetic properties. *Z. Anorg. Allg. Chem.* **2018**, *644*, 1923−1929.

(36) May, A. F.; Ovchinnikov, D.; Zheng, Q.; Hermann, R.; Calder, S.; Huang, B.; Fei, Z.; Liu, Y.; Xu, X.; McGuire, M. A. Ferromagnetism near room temperature in the cleavable van der Waals crystal Fe_5GeTe_2. *ACS Nano* **2019**, *13*, 4436−4442.

https://doi.org/10.1021/acsomega.4c01395
ACS Omega 2024, 9, 21287−21297

(37) May, A. F.; Bridges, C. A.; McGuire, M. A. Physical properties and thermal stability of $Fe_{5-x}GeTe_2$ single crystals. *Phys. Rev. Mater.* **2019**, *3*, 104401.
(38) Zhang, H.; Chen, R.; Zhai, K.; Chen, X.; Caretta, L.; Huang, X.; Chopdekar, R. V.; Cao, J.; Sun, J.; Yao, J.; Birgeneau, R.; Ramesh, R. Itinerant ferromagnetism in van der Waals $F_{e5-x}GeTe_2$ crystals above room temperature. *Phys. Rev. B* **2020**, *102*, 064417.
(39) Gao, Y.; Yin, Q.; Wang, Q.; Li, Z.; Cai, J.; Zhao, T.; Lei, H.; Wang, S.; Zhang, Y.; Shen, B. Spontaneous (anti)Meron chains in the domain walls of van der Waals ferromagnetic $Fe_{5-x}GeTe_2$. *Adv. Mater.* **2020**, *32*, 2005228.
(40) Ly, T. T.; Park, J.; Kim, K.; Ahn, H.-B.; Lee, N. J.; Kim, K.; Park, T.-E.; Duvjir, G.; Lam, N. H.; Jang, K.; You, C.-Y.; Jo, Y.; Kim, S. K.; Lee, C.; Kim, S.; Kim, J. Direct observation of Fe-Ge ordering in $Fe_{5-x}GeTe_2$ crystals and resultant helimagnetism. *Adv. Funct. Mater.* **2021**, *31*, 2009758.
(41) Wu, X.; Lei, L.; Yin, Q.; Zhao, N.-N.; Li, M.; Wang, Z.; Liu, Q.; Song, W.; Ma, H.; Ding, P.; Cheng, Z.; Liu, K.; Lei, H.; Wang, S. Direct observation of competition between charge order and itinerant ferromagnetism in the van der Waals crystal $Fe_{5-x}GeTe_2$. *Phys. Rev. B* **2021**, *104*, 165101.
(42) Ershadrad, S.; Ghosh, S.; Wang, D.; Kvashnin, Y.; Sanyal, B. Unusual magnetic features in two-dimensional Fe_5GeTe_2 induced by structural reconstructions. *J. Phys. Chem. Lett.* **2022**, *13*, 4877−4883.
(43) Jothi, P. R.; Scheifers, J. P.; Zhang, Y.; Alghamdi, M.; Stekovic, D.; Itkis, M. E.; Shi, J.; Fokwa, B. P. T. $Fe_{5-x}Ge_2Te_2$-a New exfoliable itinerant ferromagnet with high Curie temperature and large perpendicular magnetic anisotropy. *Phys. Status Solidi* **2020**, *14*, 1900666.
(44) Eguchi, R.; Ikeda, M.; Yamamoto, Y.; Goto, H.; Happo, N.; Kimura, K.; Hayashi, K.; Kubozono, Y. Observation of the superstructure in $Fe_{5-x}GeTe_2$ by X-ray fluorescence holography. *Inorg. Chem.* **2024**, *63*, 947−953.
(45) Ravel, B.; Newville, M. ATHENA, ARTEMIS, HEPHAESTUS: data analysis for X-ray absorption spectroscopy using IFEFFIT. *J. Synchrotron Radiat.* **2005**, *12*, 537−541.
(46) Hayashi, K.; Happo, N.; Hosokawa, S.; Hu, W.; Matsushita, T. X-ray fluorescence holography. *J. Phys.: Condens. Matter* **2012**, *24*, 093201.
(47) Kimura, K. X-ray fluorescence holography as a probe of hyper-ordered structures. *J. Phys. Soc. Jpn.* **2022**, *91*, 091005.
(48) Barton, J. J. Removing multiple scattering and twin images from holographic images. *Phys. Rev. Lett.* **1991**, *67*, 3106−3109.
(49) Atomic Resolution Holography Analysis Tools (Photoelectron holography and X-ray fluorescence holography). See https://osdn.jp/projects/tmcoca/releases/p14436 (accessed March 5, 2023).
(50) Sayers, D. E.; Stern, E. A.; Lytle, F. W. New Technique for Investigating Noncrystalline Structures: Fourier analysis of the extended X-Ray—absorption fine structure. *Phys. Rev. Lett.* **1971**, *27*, 1204−1207.
(51) Ishii, T. Note on the K extended X-ray absorption fine structure Debye-Waller factor. *J. Phys.: Condens.Matter* **1992**, *4*, 8029−8034.
(52) Rehr, J.; Albers, R. C. Theoretical approaches to x-ray absorption fine structure. *Rev. Mod. Phys.* **2000**, *72*, 621−654.
(53) Matsushita, T.; Muro, T.; Matsui, F.; Happo, N.; Hosokawa, S.; Ohoyama, K.; Sato-Tomita, A.; Sasaki, Y. C.; Hayashi, K. Principle and reconstruction algorithm for atomic-resolution holography. *J. Phys. Soc. Jpn.* **2018**, *87*, 061002.

https://doi.org/10.1021/acsomega.4c01395
ACS Omega 2024, 9, 21287−21297